

Iron Line Profiles in Strong Gravity

Kris Beckwith¹ and Chris Done¹

¹*Department of Physics, University of Durham, South Road, Durham DH1 3LE, UK*

Released 2004 XXXXX XX

ABSTRACT

We describe a new code which can accurately calculate the relativistic effects which distort the emission from an accretion disc around a black hole. We compare our results for a disk from $6-20 r_g$ in both Schwarzschild and extreme Kerr spacetimes with the two line profile codes which are on general release in the XSPEC spectral fitting package. These are generally accurate at the 10-20% level for this range of radii, but have some drawbacks in terms of assumptions and/or resolution. In particular we show that the assumed form of the *angular* emissivity law (limb darkening or brightening) can make significant changes to the derived line profile. Lightbending effects are *never* negligible at these radii, so the observed line is produced from a range of different emitted angles, and this can affect the derived *radial* emissivity law. The line profile is not simply determined by the well defined (but numerically difficult) physical effects of strong gravity, but is also dependent on the poorly known astrophysics of the disc emission.

Key words: accretion discs - lines: profile - relativity

1 INTRODUCTION

Material in an accretion disk around a black hole is orbiting at high velocity, close to the speed of light, in a strong gravitational potential. Hence its emission is distorted by doppler shifts, length contraction, time dilation, gravitational redshift and lightbending. The combined impact of these special and general relativistic effects was first calculated in the now seminal paper of Cunningham (1975), where he used a *transfer function* to describe the relativistic effects. The observed spectrum from an accretion disc around a Kerr black hole is the convolution of this with the intrinsic disc continuum emission.

While such models have been used to try to determine the gravitational potential from the observed accretion disk spectra (e.g. Laor & Netzer 1989; Ebisawa, Mitsuda & Hanawa 1991; Ebisawa et al. 1993; Makishima et al. 2000; Gierlinski, Maciolek-Niedzwiecki & Ebisawa 2001), these attempts suffer from our limited knowledge of the spectral shape of the intrinsic accretion disk emission (see e.g. the review by Blaes 2002). It is much easier to determine the relativistic effects from a *sharp* spectral feature, such as the iron fluorescence line expected from X-ray illumination of an accretion disc (Fabian et al. 1989). An originally narrow atomic transition is transformed into broad, skewed profile whose shape is given *directly* by the transfer function.

Observationally, evidence for a relativistically smeared iron line first came from the ASCA observation of the active

galactic nuclei (AGN) MCG-6-30-15 (Tanaka et al. 1995). Further observations showed evidence for the line profile being so broad as to require a maximally spinning black hole (Iwasawa et al. 1996). More recent data from XMM are interpreted as showing that the line is even wider than expected from an extreme Kerr disk, requiring direct extraction of the spin energy from the central black hole as well as the immense gravitational potential (Wilms et al. 2001).

Such results are incredibly exciting, but X-ray spectral fitting is not entirely unambiguous. There is a complex reflected continuum as well as the line (Nayakshin, Kazanas & Kallman 2000; Ballantyne, Ross & Fabian 2001). For an ionised disk (as inferred for MCG-6-30-15) the current models in general use (`pexriv` in the XSPEC spectral fitting package) are probably highly incomplete (Ross, Fabian & Young 1999). Complex ionised absorption also affects AGN spectra (e.g. Kaspi et al. 2002) and the illuminating continuum itself can have complex curvature rather than being a simple power law. The Galactic X-ray binary systems which are presumably the scaled down versions of the AGN and quasars, show complex X-ray continua (e.g. Gierlinski & Done 2003 and references therein).

However, in MCG-6-30-15 these issues have been examined in detail, and the results on the dramatic line width appear robust (Vaughan & Fabian 2003; Reynolds et al. 2004). Thus there is a clear requirement that the extreme relativistic effects are well modelled. There are two models which are currently widely available to the observational commu-

nity, within the `XSPEC` spectral fitting package, `diskline` (based on Fabian et al. 1989) and `laor` (Laor 1991). The analytic `diskline` code models the line profile from an accretion disc around a Schwarzschild black hole (so of course cannot be used to describe the effects in a Kerr geometry). Also, it does not include the effects of lightbending (although Fabian et al. 1989 outline a scheme for incorporating this) and hence does not accurately calculate all the relativistic effects for $r < 20r_g$ (where $r_g = GM/c^2$). By contrast, the `laor` model numerically calculates the line profile including lightbending for an extreme Kerr black hole, but uses a rather small set of tabulated transfer functions which limit its resolution and accuracy (see Section 3.3).

While there are other relativistic codes in the literature which do not suffer from these limitations, these are not generally readily and/or easily available for observers to use. There is a clear need for a fast, accurate, high resolution code which can be used to fit data from the next generation of satellites. In this paper we describe our new code for computing the relativistic iron line profile in both the Schwarzschild and Kerr metrics. We compare this with the `diskline` and `laor` models in `XSPEC` for discs which extend down to $6r_g$, and highlight both the strengths and limitations of these previous models.

2 CALCULATING STRONG GRAVITATIONAL EFFECTS

2.1 Introduction

We follow the standard approach (e.g. Cunningham 1975; Fabian et al. 1989; Fanton et al. 1997) and calculate an infinitesimal amount of flux, dF_o observed at energy, E_o due to a patch on the disk which subtends a solid angle $d\Xi$ on the image of the disc at the observer (see Fig. 1 and 2).

$$dF_o(E_o) = I_o(E_o) d\Xi = g^3 I_e(E_e) d\Xi \quad (1)$$

where the redshift factor $g = E_o/E_e$ and specific intensity in the observers and emitters frame, I_o and I_e are related through the relativistic invariant I/ν^3 . For an emission line with rest energy E_{int} , then $I_e(E_e) = \varepsilon(r_e, \mu_e) \delta(E_e - E_{int})$, where $\varepsilon(r_e, \mu_e)$ is the emissivity, which can be a function of the radius, r_e and angle, μ_e at which the photon is emitted (as defined in Figure 1). The infinitesimal flux becomes

$$dF_o(E_o) = g^4 \varepsilon(r_e, \mu_e) \delta(E_o - gE_{int}) d\Xi \quad (2)$$

The total flux can be obtained by integrating over all the entire image of the disk in the observers sky. We can write $d\Xi = d\alpha d\beta / r_o^2$ where α, β are the x, y coordinates of the image of the disc at the observer with coordinates (r_o, θ_o) (see Figure 2), such that

$$F_o(E_o) = \frac{1}{r_o^2} \int \int g^4 \varepsilon(r_e, \mu_e) \delta(E_o - gE_{int}) d\alpha d\beta \quad (3)$$

The α, β position of the image of the disc section is determined by the (covariant) angular momenta of the emitted photons, λ, q , in the azimuthal and polar directions, respectively. These are both conserved quantities, also termed constants of the motion and are defined as

$$\alpha = -\frac{\lambda}{\sin \theta_o} \quad (4)$$

$$\beta = \pm \sqrt{q^2 - \lambda^2 \cot^2 \theta_o} \quad (5)$$

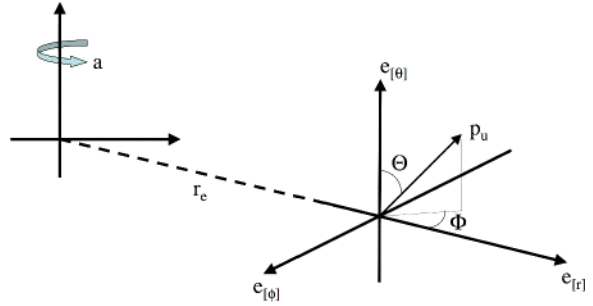


Figure 1. The coordinate system used for the disc. The emission is defined in the rest frame of the disc material. The polar and azimuthal emission angles Θ, Φ are obtained by taking the dot-products of the photon four-momentum with the basis vectors of this frame, where $\mu_e = \cos \Theta$. This disc frame can be connected to the frame which co-rotates with the black hole spacetime via a simple boost which depends on the velocity structure of the disc.

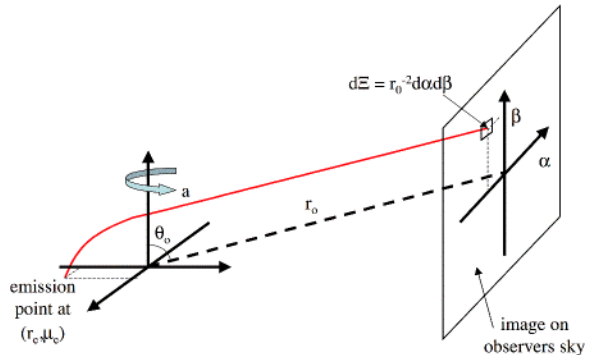


Figure 2. Diagram showing the link between the observers frame of reference and the global coordinate system defined by the black hole. Photons that are emitted from the disc at some distance r_e from the hole are seen at coordinates α, β on the image of the disc at the observer.

For a thin, Keplerian disc, these constants of motion can be written in terms of the redshift factor of the photon, g and the radius of emission, r_e and angle of emission, μ_e of the photon (as previously defined):

$$\lambda = \frac{1}{\Omega} \left(1 - \frac{e^{-\psi}}{g} \right) \quad (6)$$

$$q = \frac{r_e \mu_e}{g} \quad (7)$$

Here, Ω describes the azimuthal velocity profile of the emitting region and $e^{-\psi}$ is the 'redshift function' (Fanton et al. 1997; Martocchia 2000), which for a geometrically thin, Keplerian disc located in the equatorial plane are given by:

$$\Omega = \frac{1}{a + \sqrt{r_e^3}} \quad (8)$$

$$e^{-\psi} = \left[1 - \frac{2}{r_e} (1 - a\Omega)^2 - (r_e^2 + a^2) \Omega^2 \right]^{-\frac{1}{2}} \quad (9)$$

Thus the problem reduces to finding the area on the observers sky subtended by all parts of the disc which contribute to a given E_o .

2.2 Determination of the Solid Angle

The determination of the area at the observer is easy to calculate if light travels in straight lines as $\mu_e = \mu_o = \text{constant}$. Then

$$\alpha = \alpha(\lambda) = \alpha(r_e, g) \quad (10)$$

$$\beta = \beta(\lambda, q) = \beta(r_e, g) \quad (11)$$

Thus the solid angle in the observers frame of reference can be determined from the transformation

$$d\alpha d\beta = \frac{\partial(\alpha, \beta)}{\partial(\lambda, q)} d\lambda dq = \frac{\partial(\alpha, \beta)}{\partial(\lambda, q)} \frac{\partial(\lambda, q)}{\partial(r_e, g)} dr_e dg \quad (12)$$

This is the approach taken by the `diskline` code (Fabian et al. 1989) in XSPEC, where both $\partial(\alpha, \beta)/\partial(\lambda, q)$ and $\partial(\lambda, q)/\partial(r_e, g)$ can be determined analytically. This makes `diskline` a very fast code, but obviously limits its use in situations where there is strong lightbending.

In general, Equation (11) should include μ_e , so that $\beta = \beta(\lambda, q) = \beta(\mu_e, r_e, g)$. The first transformation $\partial(\alpha, \beta)/\partial(\lambda, q)$ can still be determined analytically as before, but the second one, from λ, q space to r_e, g space, is much more complex. Lightbending means that a range of μ_e can contribute to a given θ_o , and these emission angles can only be found by determining the full general relativistic light travel paths which link the disc to the observer. These null geodesics are given by solutions of the equations (Carter 1968; Misner, Thorne and Wheeler 1973; Chandrasekhar 1983)

$$\begin{aligned} & \pm \left[\int_{u_t}^{u_e} \frac{du}{\sqrt{U_{\lambda, q}(u)}} \mp \int_{u_t}^{u_o} \frac{du}{\sqrt{U_{\lambda, q}(u)}} \right] \\ & = \pm \left[\int_{m_e}^{m_t} \frac{dm}{\sqrt{M_{\lambda, q}(m)}} \mp \int_{m_o}^{m_t} \frac{dm}{\sqrt{M_{\lambda, q}(m)}} \right] \quad (13) \end{aligned}$$

where $u = 1/r$, $m = \cos\theta$ describe the radial and polar motion of the light travel paths and u_t, m_t denote the radial and polar turning points of the path. Equations (13) can be solved numerically, but can also be given in terms of analytic functions (Rauch & Blandford 1994; Agol 1997; Cadez et al. 1998), which enable them to be solved quickly and with arbitrary accuracy.

Several attempts at an analytic form for $\partial(\lambda, q)/\partial(r_e, g)$ including the effects of light travel paths with different μ_e exist in the literature. However, none of them are formally correct. Fanton et al. (1997) project the (μ_e, r_e, g) surface onto the (λ, q) plane. This fails as the surface in the (μ_e, r_e, g) parameter space is inherently three-dimensional, so its area is *not* given by the projection of this shape onto a two-dimensional surface¹. An alternative approach by Bao et al. (1994) attempts to calculate the transformation $(\lambda, q) \rightarrow (\mu_e, r_e, g)$ by taking the derivatives of the geodesic equations with respect to (λ, q) . There are two flaws in the approach - firstly, the equations of Bao et al. (1994) fail to take into account the properties of the turning points of the geodesic paths, (u_t, m_t) , since these are also functions of the constants of motion, $[u_t(\lambda, q), m_t(\lambda, q)]$ (see Viergutz

¹ c.f. the case of a three-dimensional sphere, which has true surface area $4\pi r^2$, but its projection onto a two-dimensional plane has corresponding surface area of only πr^2

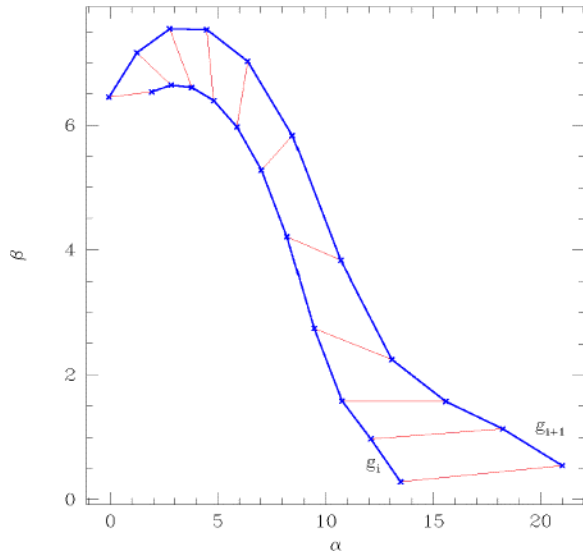


Figure 3. Heavy blue lines denote adjacent contours of constant redshift, $g_i < g_{i+1}$ on the observers sky (the α, β -plane) that define the area of the redshift bin $g = g_i + \frac{1}{2}(g_{i+1} - g_i)$ with width $dg = g_{i+1} - g_i$. Red narrow lines show examples of the divisions used to create a set of meshed trapezoids that enable the area of the redshift bin to be determined. For the purposes of clarity, this mesh is far coarser than that used in the calculations.

1993). Furthermore, as also discussed by Viergutz (1993), these derivatives may not always exist as the geodesic equations are so badly behaved.

Both Cunningham (1975) and Fabian et al. (1989) suggest a finite difference method to calculate the change in (r_e, g) with variations in (λ, q) . However, this approach can run into numerical problems as there is only a limited range of (λ, q) which can reach the observer for a given (r_e, g) pair. The transformation $\partial(\lambda, q)/\partial(r_e, g)$ is not defined at these limiting values, since we cannot evaluate the functions at both slightly larger and smaller (λ, q) . Another subtlety is that for numerical integration of the geodesic equations, the solutions can switch from those which give a direct image of the disc to those where the light travel paths orbit the black hole (higher order images). This gives a discontinuous change in α, β at the observer. If this is not recognised as a different type of image then it produces an incorrect determination of the observed flux.

An alternative approach that avoids these difficulties is a Monte-Carlo technique (see e.g. Laor 1991; Zakharov & Repin 2003). These calculate the transfer function for a set of rings within the disc $r_e \pm dr_e/2$ by following the trajectories of a finite set of photons emitted from each ring and then counting the number of photons that arrive at $\theta_o \pm d\theta_o/2$. The line profile for then extended disc is the obtained by computing a (weighted) summation of these transfer functions. Since this is a (fully) numerical approach, the issues involved with determining the partial derivatives in the transformation given by Equation (12) are avoided. However, in this approach, the accuracy of the calculation is governed by the number of photons that are emitted from each ring, the width of the ring and the angular size of the observers bin.

Instead, we develop a technique based solely on the image of the accretion disc in the α, β plane, which defines the flux received by the observer. This allows us to generate high resolution, accurate line profiles numerically while avoiding the issues surrounding the partial derivatives of Equation (12). We use the analytic solutions of Equation (13) as tabulated by Rauch & Blandford (1994) to find the complete set of light travel paths that link the accretion disk and the observer at (r_o, θ_o) . We sort these by redshift factor, and use adaptive gridding to find the boundaries on the (α, β) -plane for all lines of constant g .

Two adjacent boundaries, g_i and g_{i+1} , therefore define the area of the redshift bin $g = g_i + \frac{1}{2}(g_{i+1} - g_i)$ with width $dg = g_{i+1} - g_i$ when projected onto the (α, β) -plane (as is shown in Figure 3). We can simply determine the area of this region by dividing it up into a set of tessellating trapezoids, as shown in Figure 3, the area of each of which can be determined by a simple geometric formula. The final area of the redshift bin is determined by summing together the contributions from all such trapezoids internal to (g_i, g_{i+1}) . Each individual trapezoid is small, so that there is no significant change in r_e or μ_e (though this is not necessarily true across the total area $d\alpha d\beta$). The emissivity law can be convolved into the calculation using the emission coordinates at the centre of each trapezoid to weight its area before performing the summation over all trapezoids. This approach allows us to calculate line profiles at high spectral resolution on timescales of a few minutes on a 2GHz desktop PC.

We have extensively tested the routines that calculate the null geodesic paths against those supplied by Eric Agol (Agol 1997) and have found them to be indistinguishable. We have also compared the line profiles generated by our code to those presented previously in the literature, in particular those given by Matt, Perola & Stella (1993) and have found them to be very similar.

3 RELATIVISTIC LINE PROFILES

3.1 Introduction

We have taken a disc from $r_{min} = 6r_g$ (the minimum stable orbit for the Schwarzschild solution) to $r_{max} = 20r_g$ (beyond which strong gravitational effects become of diminishing importance) for both the Schwarzschild ($a = 0$) and maximal Kerr ($a = 0.998$) cases for $\theta_o = 5^\circ, 30^\circ, 60^\circ$ and 85° .

We compare our Schwarzschild and Kerr results with the `diskline` and `laor` codes, respectively. Since we truncate the disc at $6r_g$ then the spacetime distortions should be rather similar for these two metrics (Laor 1991). However, `diskline` does not include lightbending, so first we look at the extent of these effects in a Schwarzschild spacetime. Figure 4 shows the three-dimensional surface in (μ_e, r_e, g) for the complete set of light travel paths connecting the accretion disc to the observer. There is a considerable range of μ_e contributing to the observed emission at all inclinations. For low inclinations the effect is fairly uniform, with each radius contributing a similar range in μ_e , but with a systematic shift to larger emission angles (smaller μ_e) with smaller radii. By contrast, at higher inclinations the lightbending is strong enough to gravitationally lens the far side of the disc. This leads to a much larger range of μ_e which contribute

to the disc image at small radii. In all cases, lightbending means there is a range of μ_e which contribute to the observed disc emission, so that in general, the line profile *will* depend on the angular distribution of the emitted flux.

Fig. 5 shows the corresponding surfaces for the extreme Kerr case. Clearly they are rather similar, though there are differences, which can be seen especially at the smallest radii for 85° .

To construct the relativistic line profile, we map these surfaces on to the (α, β) plane as discussed in the previous section, forming images of the accretion disc as previously calculated by e.g. Cunningham & Bardeen (1973); Luminet (1979); Hollywood & Melia (1997); Fanton et al. (1997); Falcke, Melia, & Agol (2000). Figures 6a–d show the redshift image of the Schwarzschild disc, where the colours indicate the value of the redshift factor, g , as defined by the scale at the top of each image. The corresponding flux image (Figures 7a–d) has each redshift bin coloured by its area on the observers sky, i.e. $g^4 d\alpha d\beta$, again with the scale defined at the top of each image. Strong gravitational lensing effects can now clearly be seen in the high inclination images. Photons from the far side of the disc pass close to the black hole, so the disc image is strongly distorted (Matt, Perola & Stella 1993; Zakharov & Repin 2003). Since the area of the disc is magnified, its contribution to the observed flux should be large. However, we stress that the low inclination images *are* also affected by lightbending (see Figure 4a and 5a), though they are not magnified by gravitational lensing.

The corresponding redshift and flux images for the maximal Kerr spacetime look very similar to the Schwarzschild images, so are not shown separately.

A 'real' line profile is determined from the flux image (representing the effects of strong gravity), together with the assumed form for the emissivity (determined by the energy release and radiative transfer processes), which is generally taken as:

$$\varepsilon(r_e, \mu_e) = \varepsilon(r_e) f(\mu_e) \quad (14)$$

While the flux image is a difficult numerical problem, it depends on well known *physics*. By contrast, the emissivity laws considered have rather simple forms, but are determined by the poorly known *astrophysics* of the disc. We will consider various emissivity laws in the next section, but here we plot the effects of gravity alone, i.e. assuming a constant emissivity with both angle and radius. Figure 8 shows these profiles for both Schwarzschild and Kerr, showing the strong similarities between them for a disc from 6 – $20 r_g$.

3.2 Comparison with the Diskline Model

The `diskline` code assumes a Schwarzschild metric ($a = 0$) and additionally that light travels in straight lines (so the angular emissivity term is irrelevant). In its `XSPEC` implementation it allows both arbitrary power law $\varepsilon(r_e) \propto r^q$ and point source illumination. However, its analytic structure means that any radial emissivity law is easy to incorporate. We choose to use $q = -3$, as this is approximately the form of the gravitational energy release per unit disc area (see e.g. Zycki, Done & Smith 1989).

Figure 9 shows our line profiles assuming $f(\mu_e) = 1$ (no angular dependance of the emissivity) compared with

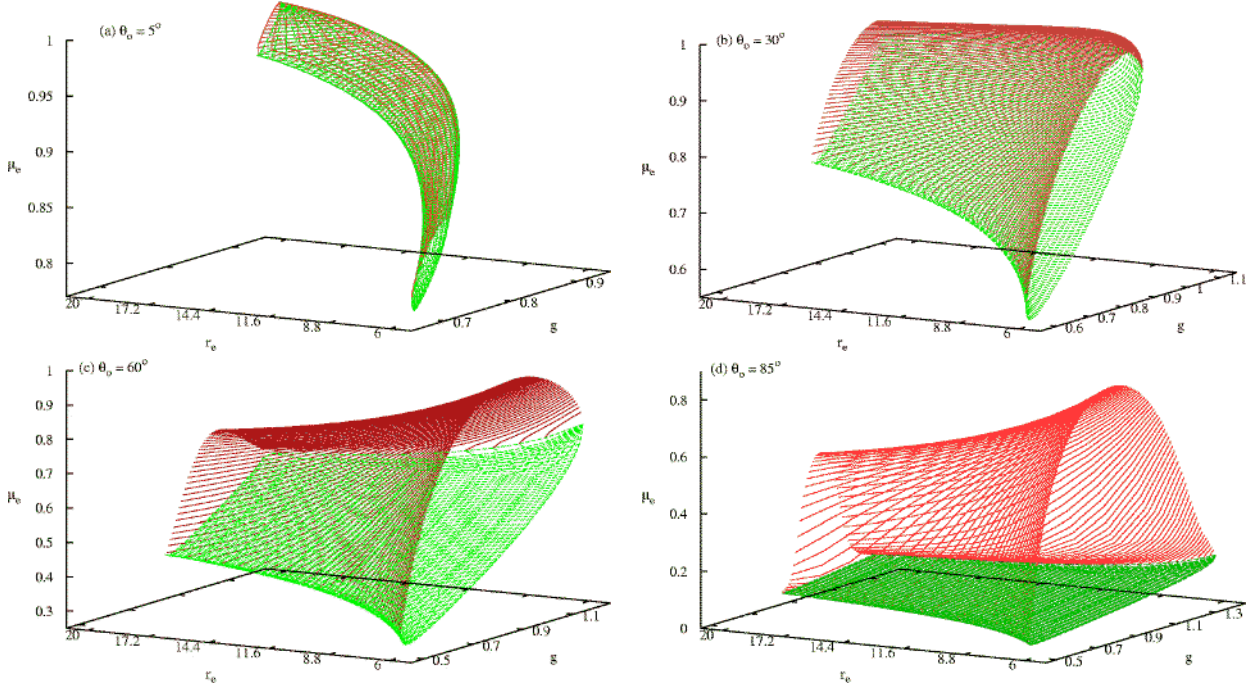


Figure 4. Surfaces in the (μ_e, r_e, g) parameter space describing geodesics that reach an observer at a given inclination for a standard accretion disk around a Schwarzschild black hole. Notice that, for every (r_e, g) pair, there are two geodesics that reach any given observer, corresponding respectively to geodesics that are emitted from the side of the disc closest to the observer (lower surface) and geodesics that are emitted from the opposite side of the disc to the observer (upper surface). These are the two geodesics referred to by Cunningham (1975).

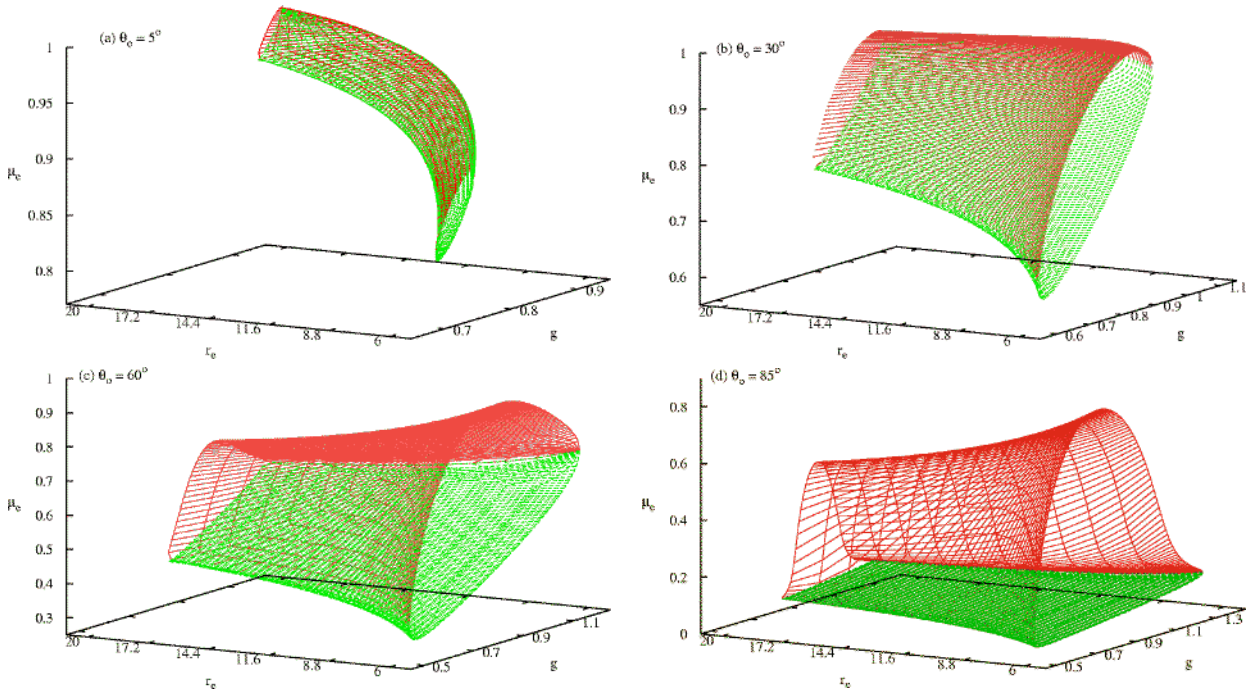


Figure 5. As in Figure 4 for a maximal ($a = 0.998$) Kerr black hole. By comparison with the Schwarzschild case, black hole spin gives subtle changes the distribution of the emission angles that solve the geodesic equations for a given (r_e, θ_e) , (r_o, θ_o) set, whilst leaving the range of energies of the observed photons largely unchanged.

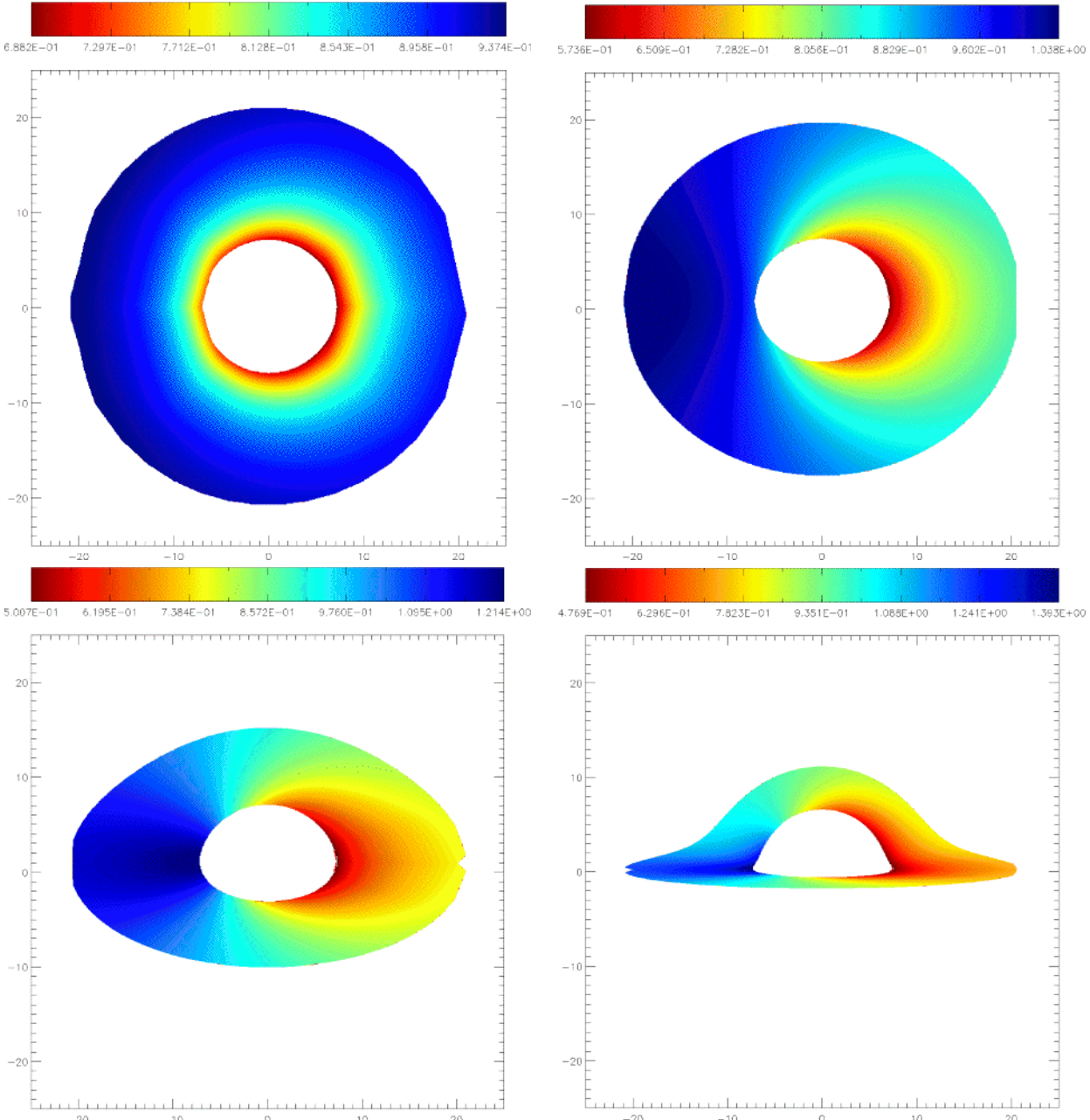


Figure 6. Redshift images of the accretion disc on the (α, β) plane for a Schwarzschild black hole, colored by the associated values of g as measured by the distant observer for $\theta_o = 5^\circ$ (top left panel); $\theta_o = 30^\circ$ (top right panel); $\theta_o = 60^\circ$ (bottom left panel); $\theta_o = 85^\circ$ (bottom right panel). Note the appearance of strong light bending effects in the $\theta_o = 85^\circ$ case, as previously reported by Matt, Perola and Stella (1993), Zakharov and Repin (2003).

those from the `diskline` code. We see that our new model matches very closely to the XSPEC `diskline` model for a nearly face on disk. Whilst the key difference between our model and `diskline` is the inclusion of light-bending effects, the impact of this is small at low inclinations if there is no angular dependance to the emissivity.

By contrast, at high inclinations, lightbending not only means that the line is formed from many different μ_e , but gravitational lensing enhances the flux from the far side of the disc. This lensing effect gives clear differences between

our model and `diskline`. The lensing magnifies the image of the far side of the disc, which has velocity mostly tangential to the line of sight, so is not strongly doppler shifted. This boosts the line profile at $g \sim 1$ (see Matt, Perola & Stella 1993). Since the line profiles are all normalised to a single photon, then this also makes the blue peak smaller.

In summary, the `diskline` model as incorporated into XSPEC produces line profiles which are accurate to $\sim 10\%$ for inclinations of less than 30° . However we caution that this excellent match is *only* obtained for the assumption of

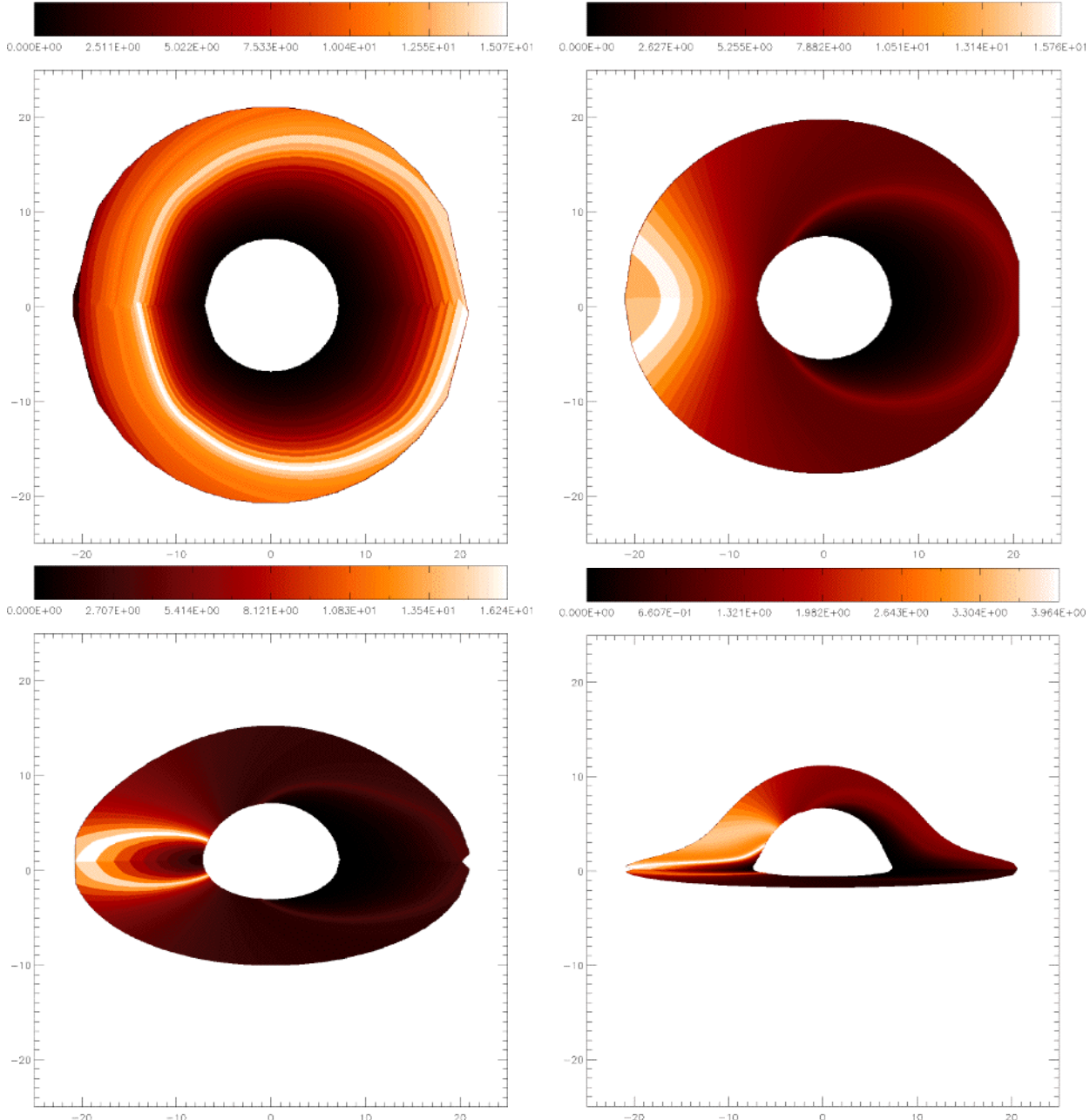


Figure 7. Flux images of the accretion disc on the (α, β) plane for a Schwarzschild black hole, colored by the $g^4 r_o^2 d\Xi = g^4 d\alpha d\beta$ component of the relativistic line profile for $\theta_o = 5^\circ$ (top left panel); $\theta_o = 30^\circ$ (top right panel); $\theta_o = 60^\circ$ (bottom left panel); $\theta_o = 85^\circ$ (bottom right panel).

constant angular emissivity. In Section 3.4 we show that a limb darkening law can give much larger distortions to the line profile even at these low inclinations. At higher inclinations the differences between `diskline` and our code become larger due to the effects of gravitational lensing, which leads to an effective redistribution in flux between the blue peak and the center of the line compared to that predicted from straight light travel paths.

3.3 Comparison with the Laor Model

By contrast, the `laor` code is written for extreme Kerr, and includes a standard limb darkening law $f(\mu_e) \propto (1+2.06\mu_e)$. The code is based on a series of Monte-Carlo calculations, where the disk is split up into a set of rings of width dr_e at r_e . Each part of the ring radiates with total emissivity (radial plus angular) given simply by the limb darkening law (i.e. no radial dependence, $q = 0$) and the line profile from that ring is built up from many light travel paths which connect the disc to the observer. This produces a series of *transfer functions* $T(r_e, E_o - gE_{int})$ at each radius, analog-

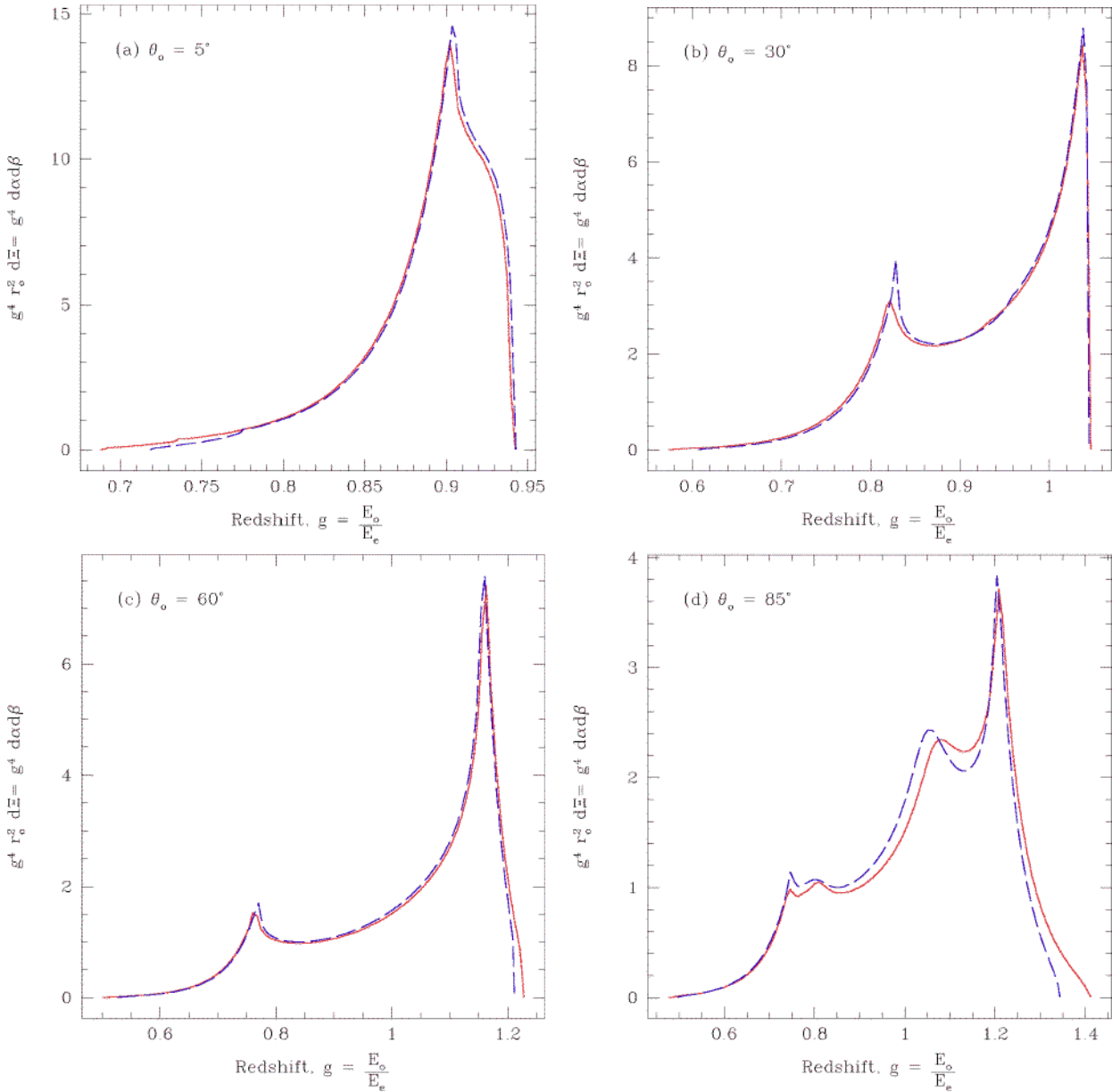


Figure 8. The $g^4 r_o^2 d\Xi = g^4 d\alpha d\beta$ component of the relativistic line profile for Schwarzschild (red solid line) and maximal Kerr (blue dashed line) black holes. Note that these profiles have not been smoothed in any way. The similarity between the Schwarzschild and Kerr spacetimes in the region $6 - 20r_g$ can be seen by comparison of the line profiles for each value of θ_o . Differences between the line profiles become apparent at high inclinations, since it is here that photons experience the strongest gravitational lensing effects and this serves to highlight the difference between the Schwarzschild and Kerr black holes.

gous to Figure 6a–d but including the limb darkening law. These tabulated transfer functions are read by the `laor` code in XSPEC and used to build a total line profile for any given radial emissivity $F_o(E_o) = \int \varepsilon(r_e)T(r_e), E_o - gE_{int}r_e dr_e d\theta$.

We compare this with our code, using a $q = -3$ emissivity for both as in the `diskline` comparisons above. We include the same limb darkening law as used by `laor` and the results are shown in Figure 10. Firstly, it is clear that there are some resolution issues in the XSPEC `laor` model, which are particularly extreme at high inclinations. The initial set of transfer functions have much higher energy resolution, so these problems reflect instead on how the transfer functions

are combined to make the total line profile. Taking these issues into account, the match between our code and `laor` is good to $\sim 10 - 20\%$ except for the highest inclination. Here our model has much more flux in the central, gravitationally lensed peak, than in the blue peak, while the `laor` model still has the blue peak with the highest flux. Indeed the gravitationally lensed peak seems to be completely absent from the `laor` model, an issue that we shall return to in a subsequent paper.

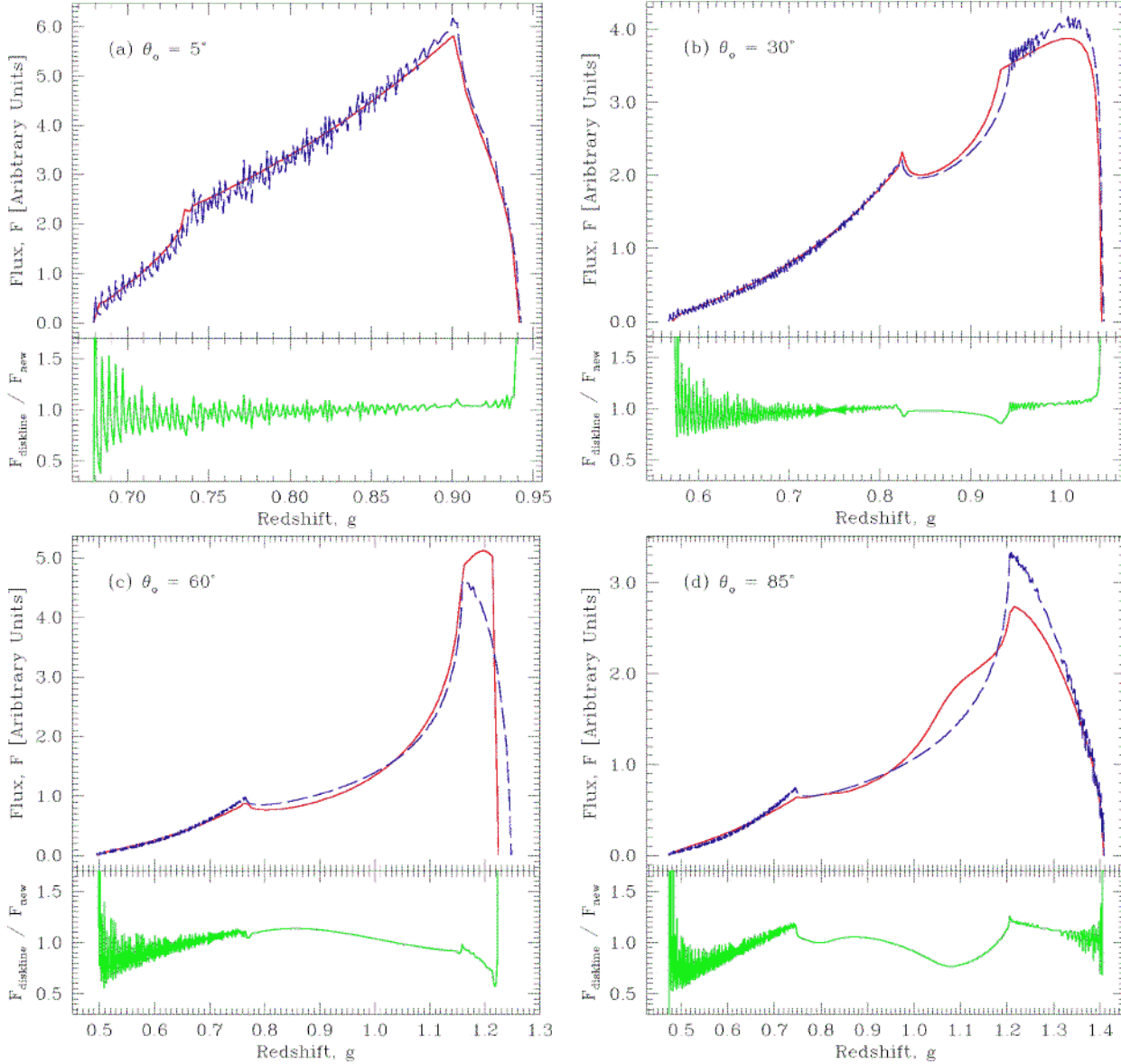


Figure 9. Comparison of the relativistic line profile computed by our model (red solid line) with that computed by the XSPEC `diskline` model (blue dashed line) for $\varepsilon(r_e) \propto r^{-3}$ and $f(\mu_e) = 1$. Our profiles are unsmoothed and all are normalised such that they contain one photon. The lower panel of each plot shows the ratio of the two models, which demonstrate that in the regions containing the majority of the total flux in the line (i.e. the blue wing), light bending can have a 40% effect on the profile shape for inclinations $> 60^\circ$. At inclinations of $< 30^\circ$, the profiles match to within 10 – 20%.

3.4 Comparison of Schwarzschild and Kerr spacetimes

Figs. 8a-d show that the line profile for a constant emissivity disc is very similar for both Schwarzschild and Kerr metrics. However, with r^0 emissivity the flux is dominated by the largest radii i.e. $20r_g$ where the differences between Schwarzschild and Kerr metrics are very small. By contrast, with a more realistic r^{-3} emissivity then the flux is weighted instead to the smallest radii at $6r_g$. Fig. 11 shows our line profile for 85° computed in both Schwarzschild and Kerr with r^{-3} and limb darkened emissivity. There are now strong differences between the lines predicted by the two spacetimes. At these high inclinations, photons from the far side

of the disc have light travel paths that take them close above the black hole, so they experience strong gravity. On these small scales, the Kerr black hole has stronger gravity than a Schwarzschild one, so there is slightly more lightbending. This can be seen from Figure 8d, where the Kerr central lensed peak is somewhat stronger than the Schwarzschild one, and the effect in Fig. 11 is much more marked as the mean emission radius is $\sim 6r_g$ rather than $20r_g$. This is then further enhanced by the limb darkening law as the strongly lensed photons typically have the smallest μ_e . The spacetime can have a strong effect on the line profile, even for a disc which only extends down to $6r_g$.

The effects of spacetime and emissivity are shown in

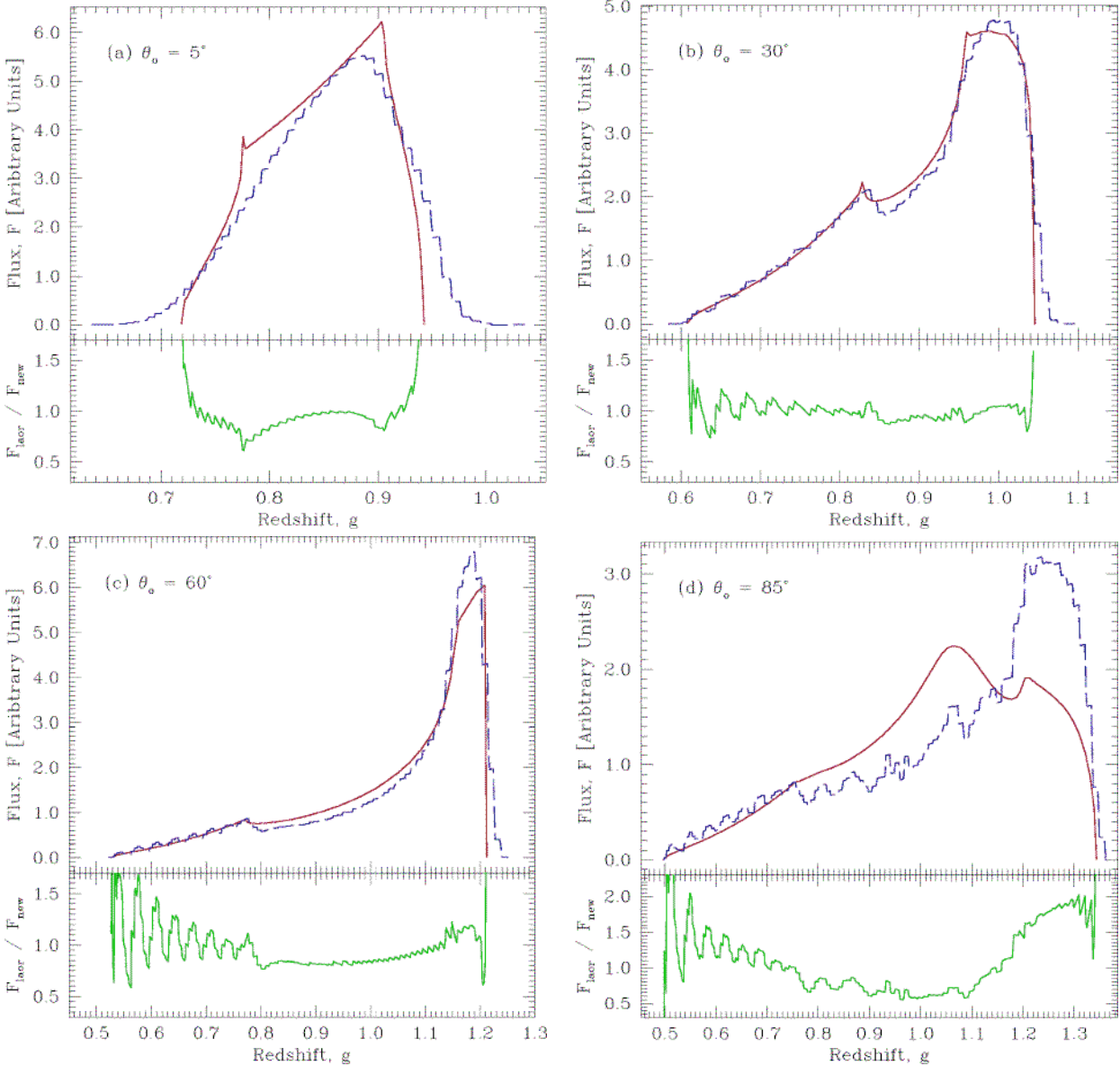


Figure 10. Comparison of the relativistic line profile computed by our model (red solid line) with that computed by the XSPEC `laor` model (blue dashed line) for $\varepsilon(r_e) \propto r^{-3}$ and $f(\mu_e) \propto (1 + 2.06\mu_e)$. Our profiles are unsmoothed and normalised such that they contain one photon. Note the resolution issues experienced by the results produced by the `laor` model, which becomes increasingly severe at high inclinations. The lower panel of each plot again shows the ratio of the two models. If we consider the case with the least resolution issues for the `laor` (that is $\theta_o = 30^\circ$), then we see that the deviation between the two models is $< 5\%$, which given the resolution issues experienced by the `laor` model even in this case, is unsurprising

Fig. 12 for the much less extreme inclination of 30° with radial emissivity of r^{-3} over 6 – $20 r_g$. The lines are (from top to bottom at the blue peak) from extreme Kerr with limb darkening, extreme Kerr with constant angular emissivity, Schwarzschild with limb darkening and Schwarzschild with constant emissivity. There is a 20% change in relative height in the blue peak between the various models. In data fitting, if the model assumed a Kerr metric with limb darkening (i.e. `laor`) while the real line was from a Schwarzschild, constant angular emissivity disc, then a χ^2 minimization would tend to match up the blue peak heights. This would result in a deficit across the red wing, pulling the *radial* emissivity into

a more centrally peaked value for q . We caution that uncertainties in the angular distribution of the line emissivity can change the expected line profile due to lightbending effects even at low/moderate inclinations for a disc extending down to $6r_g$, and we expect that these changes will be more important in stronger gravity i.e. at high inclinations and/or for a disc extending down to $1.235r_g$.

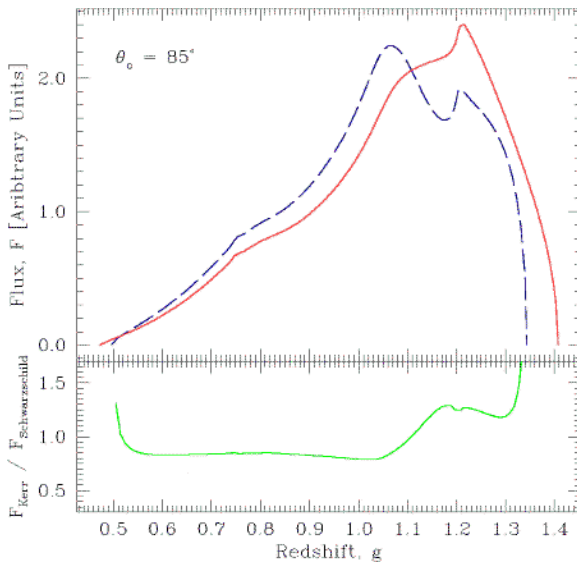


Figure 11. Comparison of the relativistic line profiles generated by our model with $\varepsilon(r_e, \mu_e) \propto r_e^{-3} (1 + 2.06\mu_e)$ for the case of a Schwarzschild (red solid line) and maximal Kerr (red dashed line) black holes.

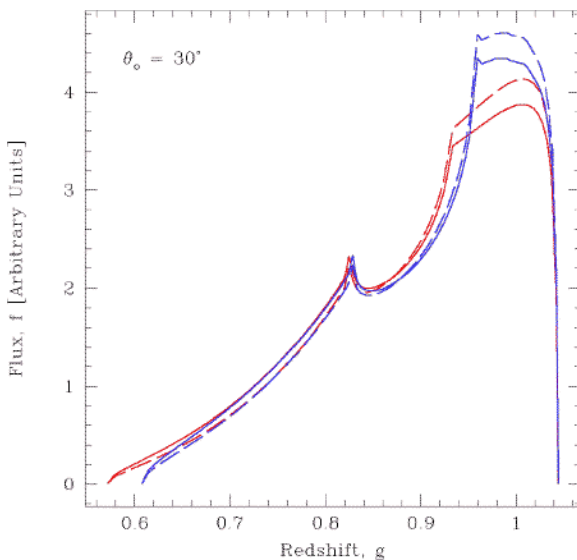


Figure 12. Comparison of the relativistic line profiles generated by our model with (a) $\varepsilon(r_e) \propto r_e^{-3}$, $f(\mu_e) = 1$ (solid lines) and (b) $\varepsilon(r_e) \propto r_e^{-3}$, $f(\mu_e) \propto (1 + 2.06\mu_e)$ (dashed lines) for the case of Schwarzschild (red lines) and maximal Kerr (blue lines) black holes. All profiles are normalised such that they contain one photon. Note the large change in the relative heights of the blue wing between the various models.

4 CONCLUSIONS

Recent observational studies have provided evidence of highly broadened fluorescent iron $K\alpha$ lines, in particular from the AGN MCG-6-30-15 where the line is so broad that Wilms et al. (2001) conclude that it requires direct extraction of black hole spin energy by magnetic fields as well as

the immense gravitational energy of an extreme Kerr black hole. However, such conclusions can only be as robust as the models and techniques from which they were derived. Leaving aside issues regarding the extraction of the iron $K\alpha$ line profile from the underlying continuum and reflected emission, the models of the strong gravitational effects that are used to fit the data and determine the properties of this line are over a decade old. They either fail to incorporate known gravitational effects into the properties of the line (the **XSPEC diskline** model adapted from Fabian et al. 1989) or have rather poor resolution, making them unsuitable for fitting current moderate and high resolution X-ray spectra (the **XSPEC laor** model adapted from Laor 1991). Increased computer power means that it is now possible to do a complete calculation of the line profiles at high resolution. We describe our new code to solve this problem, which uses fully adaptive gridding to map the image of the disc at the observer using the analytic solutions of the light travel paths. This is a very general approach, so the code can easily be modified to incorporate different emission geometries.

We show results from our code for a disc between $6-20 r_g$ with radial emissivity $\propto r^{-3}$ in both Schwarzschild and Kerr metrics, comparing these with the **diskline** and **laor** models in **XSPEC**. Lightbending is *always* important, in that the image of the disc at the observer *always* consists of a range of different emission angles. This means that the angular dependance of the emitted flux can make significant changes to the derived line profile. While calculating the strong gravity effects is a difficult numerical problem, the underlying physics is well known. By contrast, the *angular* emissivity is an astrophysical problem, and is not at all well known as it depends on the ionization state of the disc as a function both of height and radius. Figure 12 demonstrates the effect of this unknown astrophysics folded through both Schwarzschild and extreme Kerr spacetimes, showing there can be a significant difference in the ratio of the blue-to-red peak heights simply from the assumed angular emissivity. Before we can use the line profiles to provide a sensitive test General Relativity, to probe the underlying physics, we will need to have a much better understanding of the astrophysics of accretion.

In a subsequent paper we will describe the implementation of this code into **XSPEC** so that it can be freely used by the observational community. We will also show results for the extreme Kerr region from $1.23-6 r_g$, including effects from higher order images, formed by photons which orbit the black hole!

REFERENCES

- Agol E.; Ph.D. thesis, 1997, Univ. California, Santa Barbara.
- Ballantyne, D.R.; Ross, R.R.; Fabian, A.C. MNRAS 201, 327, 10.
- Bao, G.; Hadrava, P.; Ostgaard, E.; ApJ, 1994, 435, 55.
- Blaes, O.M.; Physics Fundamentals of Luminous Accretion Disks Around Black Holes in "Accretion Disks, Jets, and High Energy Phenomena in Astrophysics", Proceedings of Session LXXVIII of Les Houches Summer School, Chamonix, France, August 2002.

Cadez, A.; Fanton, C.; Calvani, M.; NEWA Vol. 3, No. 8, 647.

Carter, B.; PhRv, 1968, 174.1559C.

Chandrasekhar, S.; *The Mathematical Theory of Black Holes*, Oxford University Press, N.Y., 1983.

Cunningham, C.T.; ApJ, 1975, 202, 788

Cunningham, C.T.; Bardeen, J. M.; ApJ, 1973, 183, 237

Ebisawa, Ken; Mitsuda, Kazuhisa; Hanawa, Tomoyuki; ApJ, 1991, 367, 213

Ebisawa, Ken; Makino, Fumiyoshi; Mitsuda, Kazuhisa; Belloni, Tomaso; Cowley, Anne P.; Schmidtke, Paul C.; Treves, Aldo; ApJ, 1993, 403, 684

Fabian, A.C.; Rees, M.J.; Stellar, L.; White, N. E.; MNRAS 1989, 238, 729.

Falcke, Heino; Melia, Fulvio; Agol, Eric; ApJ, 2000, 528, L13

Fanton, C.; Calvani, M.; de Felice, F.; Cadez, A.; PASJ 1997, 49, 159

Gierlinski, Marek; Done, Chris; MNRAS 2003, 342, 1083.

Gierlinski, Marek; Maciolek-Niedzwiecki, Andrzej; Ebisawa, Ken; MNRAS 2001, 325, 1253.

Hollywood, J.M.; Melia, F.; ApJ 1997, 112, 423.

Iwasawa, K.; Fabian, A.C.; Reynolds, C. S.; Nandra, K.; Otani, C.; Inoue, H.; Hayashida, K.; Brandt, W.N.; Dotani, T.; Kunieda, H.; Matsuoka, M.; Tanaka, Y.; MNRAS 1996, 282, 1038.

Kaspi, S. et al.; ApJ 2002, 574, 643

Laor, A.; ApJ 1991, 376, 90.

Laor, A.; Netzer, H.; MNRAS 1989, 238, 897.

Luminet, J-P.; A&A 1979, 75, 228.

Makishima, Kazuo; Kubota, Aya; Mizuno, Tsunefumi; Ohnishi, Tomohisa; Tashiro, Makoto; Aruga, Yoichi; Asai, Kazumi; Dotani, Tadayasu; Mitsuda, Kazuhisa; Ueda, Yoshihiro; Uno, Shin'Ichiro; Yamaoka, Kazutaka; Ebisawa, Ken; Kohmura, Yoshiki; Okada, Kyoko; ApJ 2000, 535, 632.

Martocchia, A.; PhD Thesis, 2000, SISSA-ISAS, Trieste

Matt, G.; Perola, G.C.; Stella, L.; A&A, 1993, 267, 2, 643.

Misner, C. S.; Thorne, K. S.; Wheeler, J. A.; *Gravitation*, W H Freeman, 1973.

Nayakshin, Sergei; Kazanas, Demosthenes; Kallman, Timothy R. ApJ 2000, 537, 833.

Rauch, K. P.; Blandford, R.D.; ApJ, 1994, 421, 46.

Reynolds C.S., Wilms, J., Begelman, M.C., Staubert R., Kendziorra E., MNRAS 2004 in press (astro-ph/0401305)

Ross, R.R.; Fabian, A.C.; Young, A.J.; MNRAS 1999, 306, 461.

Tanaka, Y.; Nandra, K.; Fabian, A.C.; Inoue, H.; Otani, C.; Dotani, T.; Hayashida, K.; Iwasawa, K.; Kii, T.; Kunieda, H.; Makino, F.; Matsuoka, M. Nature, 1995, 375, 659.

Fabian, A. C. Vaughan, S. MNRAS 2003, 340, L28

Viergutz, S. U.; A&A, 1993, 272, 355.

Wilms, J.; Reynolds, Christopher S.; Begelman, Mitchell C.; Reeves, James; Molendi, Silvano; Staubert, Rdiger; Kendziorra, Eckhard; MNRAS 2001, 328, L27.

Zakharov, A. F., Repin, S. V. A&A, 2003, 406, 7.

Zycki, Piotr T.; Done, Chris; Smith, David A.; MNRAS 1998, 301, 231.